Structural, electronic and vibrational properties of tetragonal zirconia under pressure: a density functional theory study

2009 J. Phys.: Condens. Matter 21 485404

(http://iopscience.iop.org/0953-8984/21/48/485404)

IOP Publishing Journal of Physics: Condensed Matter

J. Phys.: Condens. Matter **21** (2009) 485404 (12pp) doi:10.1088/0953-8984/21/48/485404

Structural, electronic and vibrational properties of tetragonal zirconia under pressure: a density functional theory study

Victor Milman[1], Alexander Perlov[1], Keith Refson[2], Stewart J Clark[3], Jacob Gavartin[1] and Bjoern Winkler[4]

[1] Accelrys, 334 Science Park, Cambridge CB4 0WN, UK
[2] Rutherford Appleton Laboratory, Chilton, Didcot, Oxfordshire OX11 0QX, UK
[3] Department of Physics, University of Durham, South Road, Durham DH1 3LE, UK
[4] Institut für Geowissenschaften, Abteilung Kristallographie, Johann Wolfgang Goethe-Universität Frankfurt, Altenhöferallee 1, D-60438, Frankfurt am Main, Germany

E-mail: vmilman@accelrys.com

Received 23 September 2009
Published 6 November 2009
Online at stacks.iop.org/JPhysCM/21/485404

Abstract

We present the results of a plane wave based density functional study of the structure and properties of tetragonal zirconia in the range of pressures from 0 to 50 GPa. We predict a transition to a fluorite-type cubic structure at 37 GPa which is likely to be of a soft mode origin and is accompanied by a power law decrease of the frequency of the Raman-active A_{1g} mode. A detailed study of the pressure effect on phonon modes is given, including theoretical Raman spectra and their pressure dependence. Our results provide a consistent picture of the pressure-induced phase transition in tetragonal zirconia.

1. Introduction

Zirconia, ZrO_2, is an extremely important ceramic material for modern technological applications. It has useful mechanical properties for manufacturing of medical devices [1], and generally excellent characteristics for engineering applications [2]. One of the most important features that define the mechanical properties of zirconia is the transformation toughening mechanism [3]. At ambient pressure, ZrO_2 has three polymorphs, cubic (c-ZrO_2), tetragonal (t-ZrO_2) and monoclinic (m-ZrO_2). Phase transformations between cubic and tetragonal, and tetragonal and monoclinic phases occur on cooling from high temperatures. Remarkably, the ground state monoclinic phase has an atomic density only 96% of that of the cubic phase and 97% of that of the tetragonal phase. It is this anomalous property that makes transformation toughening possible. In view of this, the understanding of the interplay between mechanical properties of zirconia and its density becomes of paramount importance. A number of phase transformations in ZrO_2 are known to occur under hydrostatic pressure; for example, the monoclinic phase undergoes transitions to different orthorhombic phases upon compression [4]. The complete P–T phase diagram of zirconia [5, 6] demonstrates a rich variety of transformations that are possible in this system in response to changes in external parameters. These transformations are responsible for the high fracture toughness of zirconia based ceramics, although properties of actual engineering materials are affected also by structural defects, crystallite size, sample treatment history, etc.

There is a long history of theoretical studies of properties and phase transformations of ZrO_2. Density functional theory (DFT) is currently the method of choice for first-principles studies of crystalline materials, and a number of DFT studies address fundamental issues of structure and properties of various phases of zirconia [7, 8]. Lattice dynamics is one of the central issues in such investigations, since it is expected that many transformations in the ZrO_2 phase diagram are related to the soft phonon mode mechanism [9].

An important issue which arises when one compares theoretical and experimental results is that the DFT studies are usually performed in the athermal limit, $T = 0$ K. Most phases of ZrO_2 are difficult to stabilize at low temperatures without applying pressure or introducing dopants. The situation is more promising in the case of the tetragonal modification,

which can be stabilized in nanocrystalline form at ambient pressure and room temperature without doping. Recent experimental studies probed a number of important structural and vibrational properties of t-ZrO_2 [4, 5] including pressure-induced changes in its phonon spectrum [4]. In spite of these investigations a number of open issues remain, in particular related to the assignment of vibrational modes. Therefore, a further analysis of the pressure-induced changes in the phonon spectrum as related to the suggested high pressure phase transition [4] is required.

The present work is focused on the theoretical study of structure and properties of t-ZrO_2 under hydrostatic compression, with particular emphasis on phonon frequencies and Raman spectra. It has been suggested that external pressure removes tetragonal distortions and the structure transforms to a cubic modification via most probably a soft mode mechanism [4]. The main experimental technique used to diagnose a soft mode behaviour is Raman spectroscopy. We present the first DFT results on the pressure dependence of Raman frequencies and intensities and use these theoretical data to interpret experimental findings.

The overall structure of the paper is as follows. Section 2 presents the computational set-up of the current investigation. We then present in section 3 our results for properties of t-ZrO_2 at ambient pressure and provide a comprehensive critical review of the available experimental and theoretical data on the structure, compressibility, elastic constants, Born effective charges, dielectric permittivity, and phonon frequencies of this polymorph. The accuracy of these results allows us to proceed with the study of the effect of compression on the structure and properties (section 4), and this is followed by conclusions.

2. Computational methodology

The tetragonal modification of ZrO_2 has space group 137 ($P4_2/nmc$) with two formula units per cell. In the setting that corresponds to the origin choice 1 as defined in [10] there is a Zr atom located on the Wyckoff position 2*a* (0 0 0), and an O atom located on the Wyckoff position 4*d* (0 0.5 O_z). The structure is defined by three parameters: lattice constants a and c, and the z coordinate of the oxygen atom, O_z [11]. The actual tetragonal phase represents only a slight modification of the fluorite structure of the cubic form c-ZrO_2. The deviation from the ideal cubic arrangement is described via the tetragonal distortion of the cell parameters, $A = \frac{c}{a\sqrt{2}}$, and the internal distortion, $d_z = O_z - 0.25$. The cubic setting is characterized by $A = 1$ and $d_z = 0$.

All calculations were carried out using the DFT based CASTEP code [12, 13]. The local density approximation, LDA, is used to represent the exchange–correlation functional in the DFT formalism. It is known that for transition metal oxides a gradient-corrected approximation, GGA, to the exchange–correlation functional does not improve on the LDA description; the resulting structures overestimate bond lengths and produce too low phonon frequencies [14, 15]. On the other hand, GGA can produce more accurate formation energies, as was shown for zirconia polymorphs [16]. The pressure induced phase transition studied here relies exclusively on the effect of pressure on the crystal structure, electronic structure and vibrational properties and does not make use of relative energies of different phases; hence we adopted the LDA approach.

The electron–ion interaction was represented in our calculations by norm-conserving pseudopotentials; the reference configurations for valence electrons were $4s^24p^64d^25s^2$ for zirconium (cut-off radii of 1.58, 1.73, 1.79 and 1.72 a.u., respectively) and $2s^22p^4$ for oxygen (cut-off radii of 1.34 and 1.53 a.u., respectively). Pseudopotentials were generated using the designed nonlocal pseudopotential scheme of Rappe *et al* [17, 18] which was used to guarantee accurate valence states in unfrozen semicore potentials.

A plane wave basis set with the energy cut-off of 750 eV was used to expand the wavefunctions. An 8 × 8 × 6 Monkhorst–Pack grid [19] was used for Brillouin zone integration (30 points in the irreducible part of the Brillouin zone). The SCF convergence criterion was set to 1×10^{-8} eV/atom. Lattice parameters were converged to 2×10^{-5} Å and fractional atomic coordinates to 1×10^{-5} as compared to calculations using a higher energy cut-off of 900 eV and a more accurate k-point grid of 14 × 14 × 10 (140 irreducible points). A smaller set of k-points, 5 × 5 × 3 (12 irreducible points), has been used in earlier studies (e.g., [8, 14, 20, 21]). We found that this setting can affect cell parameters by as much as 0.001 Å and does not provide converged results for the phonon frequencies and dielectric properties that are sensitive to the crystal structure.

The pressure response of t-ZrO_2 was studied by calculating its P—V equation of state, EOS, for applied pressures up to 50 GPa. The lattice parameters and oxygen position were optimized at each value of the external pressure, so that the volume could be determined. The structures were considered converged when the z component of the force on oxygen atom was less than 0.0005 eV $Å^{-1}$, and the maximum component of the stress tensor was less than 0.01 GPa. The resultant EOS was fitted using the third-order Birch–Murnaghan analytical expression [22] to produce the bulk modulus, B, and its pressure derivative, B'. Physical properties of t-ZrO_2 including the band structure, optical properties, vibrational frequencies, dielectric permittivity, Born charges, and infrared and Raman intensities were calculated for each point of the EOS.

These structural optimizations yield an equation of state in the 'athermal limit', where the effect of both zero-point energy and temperature is neglected. The *quasi-harmonic approximation* models a thermal correction under the assumption that the dominant contribution arises from the change in vibrational free energy under thermal expansion due to the volume dependence of the phonon frequencies. Using the results of our lattice dynamics calculations at the Γ point we computed the vibrational free energy as a function of volume. This gives a zero-point and thermal contribution to the pressure of 2.2 GPa, in the pressure range from 0 to 30 GPa. However the quasi-harmonic approximation is not valid in the vicinity of a soft mode phase transition, where anharmonicity is large and the harmonic expression for the vibrational free energy does not apply. The contribution of the remaining hard

modes which do not exhibit any large anomaly through the phase transition (see figure 6) will remain roughly constant, but there is no effective means within the scope of the theory used here to compute the soft mode contribution. Consequently we choose to report pressures in the text and figures in the *athermal* limit unless stated otherwise.

Variational density functional perturbation theory, DFPT, was used to evaluate the lattice dynamics and the response to an electric field [23]. Raman activities were computed using a hybrid method combining density functional perturbation theory with finite displacements. The Raman activity tensor of a mode is given by the derivative of the dielectric permittivity tensor with respect to the mode amplitude. This was evaluated using a numerical approximation of the central difference between permittivity tensors computed using DFPT at geometries displaced from equilibrium by small positive and negative amplitudes according to the mode eigenvector. This method is similar to that of Porezag and Pedersen [24] except for our use of DFPT to compute the dielectric permittivity.

There exist a large body of experimental and theoretical results for t-ZrO_2 properties at ambient conditions. It should be noted that comparisons of theoretical data to experiment can be difficult since some of the experimental results refer to materials stabilized by impurities, or to high temperature properties, while calculations are performed on a pure material at 0 K. Nevertheless a comparison of our results to other available data can be used to judge the accuracy of the current zero-pressure calculations.

There is little information about the behaviour of the tetragonal phase of pure zirconia under pressure [4, 5]. The main goal of the subsequent discussion is to analyse the high pressure behaviour in connection with the changes in the phonon spectrum and their relationship to pressure-induced phase transitions. An analysis of the Raman mode evolution [4] based purely on experimental data was not sufficient to explain the experimentally observed transition from the tetragonal to cubic modification [5].

3. Properties of tetragonal zirconia at ambient pressure

This section presents our results for various lattice properties of t-ZrO_2 at zero pressure in comparison with experimental data and other DFT results. Such an analysis establishes the level of expected accuracy of the present calculations and is a necessary prerequisite for a phase transition study.

3.1. The structure of tetragonal zirconia

There are a wealth of experimental reports on the structure t-ZrO_2; however, care needs to be exercised in selecting the structure that can be used to validate theoretical results for pure zirconia in the athermal limit. Pure t-ZrO_2 has been studied using single-crystal x-ray diffraction at high temperature [11] and later at room temperature [4]. A neutron powder diffraction study of pure t-ZrO_2 has been performed at room temperature [25] and down to cryogenic temperatures [26, 27]; the results can be compared to those from neutron powder diffraction analysis of yttria-stabilized t-ZrO_2 [28]. A compilation of experimentally reported structural parameters is given in table A.1. It has to be noted that experimental results for nanocrystalline zirconia can exhibit a strong dependence of structural parameters and vibrational frequencies upon the crystallite size. This size has to be sufficiently small for the tetragonal phase to stabilize, but not so small as to distort bulk-like properties. It appears from experimental x-ray diffraction and Raman spectroscopy study that the recommended crystallite size range is 10–20 nm [29, 30]. We suggest that the neutron diffraction results obtained at 5 K for samples with the grain size of 13 nm provide the most accurate description of the structure of pure t-ZrO_2 [27]. This structure is characterized by $a = 3.5742(3)$ Å, $c = 5.1540(8)$ Å, with tetragonal distortion parameters $A = 1.0196$ and $d_z = 0.0473(4)$.

DFT studies of zirconia polymorphs have a long history. The structures of cubic and tetragonal modifications are fairly simple and require only modest computational resources, and hence have been studied since the early days of DFT applications to solid state problems. A number of DFT results for t-ZrO_2 published in the last two decades are collected in table A.1 and compared to experimental data. Table A.1 groups LDA and GGA results separately and the underbinding effect of GGA can be seen clearly since the cell volume is overestimated by 5–6%. LDA overbinding errors are less pronounced—the volume is underestimated by about 1%, a fraction of the GGA error. Our LDA result gives $a = 3.5654$ Å, $c = 5.1258$ Å, $A = 1.0166$ and $d_z = 0.0441$ in good agreement with experiment and with other accurate LDA calculations.

Table A.1 shows a similarity between converged theoretical studies that use different pseudopotential schemes: the projector augmented wave method (PAW), norm-conserving pseudopotentials (NCP) or ultrasoft pseudopotentials (USP). The results of pseudopotential calculations also agree well with the all-electron FLAPW data. This indicates that there is no transferability issue in well converged pseudopotential DFT calculations. This compilation of structural data also provides a guide to the sensitivity of the results obtained to such parameters as temperature and doping in the case of experimental data, and the k-point sampling and basis set size in the case of calculations.

3.2. Compressibility and elastic constants

We compare calculated elastic characteristics of t-ZrO_2 to known data in order to confirm that the response of the lattice to applied strain is reproduced accurately in DFT calculations. Available experimental and DFT results for mechanical properties and single-crystal elastic constants of tetragonal ZrO_2 are summarized in tables A.2 and A.3, respectively. The bulk modulus of single-crystalline t-ZrO_2 can be estimated at about 190(10) GPa from experimental studies, and our calculated values of 200(2) GPa in the athermal limit and 183(2) GPa taking into account quasi-harmonic corrections are in good agreement with this estimate and with other theoretical results (table A.2).

Voigt-averaged results for B and G in table A.2 represent an upper limit for polycrystalline moduli. Alternative

averaging schemes of Reuss and Hill were applied to our calculated elastic constants and produced respectively (all in GPa): $B_R = 212$, $B_H = 217$, $G_R = 76$, and $G_H = 89$. The Poisson ratio and Young modulus are strongly orientation dependent, as indicated in table A.2; our results agree well with the scarce data available for polycrystals.

Single-crystal elastic constants of t-ZrO_2 were calculated by applying finite strains and linearly fitting the calculated strain–stress dependences as described in [31]. The internal degrees of freedom are optimized for each strained structure. These calculations were carried out in two different ways: (i) using the correct crystal symmetry, where strained structures possessed the tetragonal symmetry reduced in accordance with the applied strain; and (ii) using the P1 version of the structure. The latter approach was utilized to account for the possible softening of elastic constants as a result of symmetry breaking under external stress. The effect of associated relaxations resulted in a decrease of the value of C_{13} by about 10 GPa and had very little effect on any other elastic constant. The theoretical single-crystal elastic constants are given in table A.3 in comparison to other published results. The bulk modulus as obtained from C_{ij} coefficients is 212(2) GPa and thus is in reasonable agreement with the EOS result.

It is clear from table A.3 that the bulk modulus evaluated from experimental elastic constants [32] is considerably lower than our calculated value and experimental estimates from hydrostatic compression (table A.2). The difference may be related to the fact that the experiment [32] was conducted on a ceria doped material. One could also note that the technique relies on the reference value of the Young modulus in addition to the diffraction data. The single-crystal Young modulus is orientation dependent, and according to our results its value is between 248 GPa (perpendicular to the c axis) and 320 GPa (along the c axis). If we multiply the data from [32] by a scaling factor to account for a different value of the Young modulus, we get some C_{ij} components and the bulk modulus in better agreement with DFT calculations. However, the discrepancy for the off-diagonal terms remains large or becomes worse, suggesting that either this technique is not sufficiently accurate for determining elastic constants of t-ZrO_2, or that ceria doping has a strong effect on elastic properties.

The two most recent GGA calculations [33, 34] strongly disagree with each other as regards nearly all components of the elastic constants tensor (table A.3). It is likely that the k-point sampling used in [33] is not sufficiently accurate; it results in an overestimated tetragonal distortion A (table A.1) and strongly underestimated elastic constants for the tetragonal phase.

Our LDA result for elastic constants is consistent with earlier LDA calculations [35] and with the measured bulk modulus, and represents a reliable estimate of t-ZrO_2 elastic properties.

3.3. Born effective charge tensors

The Born effective charge tensor Z^{*k}_{ij} can be defined in two equivalent ways. The charge can be thought of either as a force in the direction i on the atom k as a result of applying a unitary electric field along the direction j, or as the induced polarization in the direction i due to the unitary displacement in the direction j of all atoms k. The Born effective charge tensors are diagonal in the high symmetry structure of t-ZrO_2 [20]. The charge tensor of Zr atoms is diagonal with only two independent components, along and perpendicular to the c axis (Z^{*Zr}_{11} and Z^{*Zr}_{33}). The Born effective charge tensor of O atoms is diagonal with three inequivalent components, Z^{*O}_{11}, Z^{*O}_{22} and Z^{*O}_{33}.

Table 1. Born charges of tetragonal ZrO_2.

	LDA[a]	LDA[b]	LDA[c]
Z^{*Zr}_{11}	5.75	5.74	5.89
Z^{*Zr}_{33}	5.09	5.15	5.11
Z^{*O}_{11}	−3.53	−3.52	−3.70
Z^{*O}_{22}	−2.22	−2.49	−2.19
Z^{*O}_{33}	−2.53	−2.57	−2.56

[a] USP calculations [14].
[b] NCP calculations using ABINIT [20].
[c] NCP calculations, present result.

We present calculated LDA values at ambient pressure in table 1. Our data are in good agreement with the previous results and reproduce well the strong anisotropy of the Born effective charge tensor on oxygen atoms. The discrepancy between our results and earlier findings [14, 20] is well within the range that can be attributed to differences in the theoretical ground state structures.

3.4. The dielectric permittivity tensor

The frequency-dependent dielectric tensor of tetragonal ZrO_2 is diagonal and has two independent components: $\varepsilon_{xx} = \varepsilon_{yy}$ perpendicular to the c axis, and ε_{zz} along the c axis. There are two contributions to the dielectric tensor, electronic and lattice (phonon). The static value, ε^0, includes both contributions while the optical limit, ε^∞, includes only the electronic contribution. Available LDA results for these properties are compared in table 2. The results from [14] include only the lattice contribution, $\varepsilon^0 - \varepsilon^\infty$.

The best, although approximate, way to compare calculated single-crystal results to experimental data obtained on polycrystalline samples is to average the components of the computed tensor to produce $\bar{\varepsilon} = \frac{2\varepsilon_{xx}+\varepsilon_{zz}}{3}$. The results are included in table 2 and show a qualitative agreement with other calculations and with experiment. Overestimation of the dielectric tensors illustrated in table 2 is common for the LDA level of theory [20].

The asymmetry of the static dielectric tensor is clearly due to the lattice contributions from IR-active modes, since the electronic contribution ε^∞ is nearly isotropic.

3.5. Phonon frequencies at the Γ point

An accurate description of phonon frequencies is a stringent test for a theoretical model. There are a number of

Table 2. Dielectric permittivity tensors of tetragonal zirconia.

	LDA[a]	LDA[b]	LDA[c]	Experiment[d]
ε^0_{xx}	—	48.10	54.58	
ε^0_{zz}	—	20.31	20.23	
ε^0_{xx}-ε^{xx}_∞	41.6	42.36	48.54	
ε^0_{zz}–ε^∞_{zz}	14.9	15.03	14.82	
$\bar{\varepsilon}^0$	—	38.84	43.13	34.5–39.8
ε^∞_{xx}	—	5.74	6.04	
ε^∞_{zz}	—	5.28	5.41	
$\bar{\varepsilon}^\infty$	—	5.59	5.83	4.2–4.9

[a] USP calculations; only the lattice contribution is reported [14].
[b] NCP calculations using ABINIT [20].
[c] NCP calculations, present result.
[d] Quoted from [20].

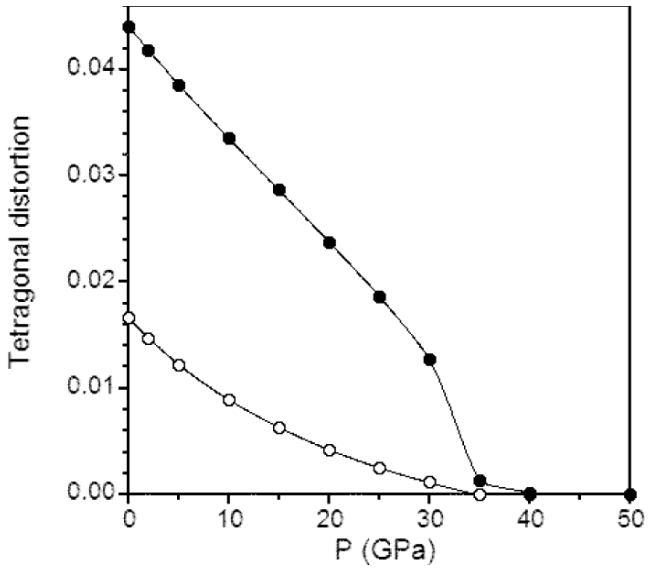

Figure 1. Pressure dependence of the tetragonal distortion characteristics, $A - 1$ (open circles) and d_z (solid circles). A quasi-harmonic correction of 2.2 GPa (at 300 K) is not included in the pressure.

experimental data on vibrational modes of tetragonal zirconia from IR and Raman spectroscopy [36–39], as well as a body of model [36, 40] and DFT [14, 20] calculated results. However, a controversy still exists as regards the phonon mode assignment. An effort at resolving this issue has been offered in [36] and independently in [20], but the resulting assignments still do not agree with each other.

Group theoretical analysis of optical modes (e.g., using the Bilbao Crystallographic Server [41]) shows that there are six Raman-active modes (A_{1g}, $2B_{1g}$, $3E_g$), three IR-active modes (A_{2u}, $2E_u$), and a silent mode (B_{2u}) in tetragonal zirconia. Experiments have been performed mostly on tetragonal zirconia stabilized with dopants which explains the scatter of experimental data reported in table 3. The most accurate results available are from the Raman spectra of a pure tetragonal phase [4, 36].

Our results for phonon frequencies are in good agreement with the earlier LDA calculations and with experimental data (table 3). Note that the GGA frequencies [8] are much less accurate than the LDA ones for both IR- and Raman-active modes, which supports our choice of the LDA functional for this study. The results of the symmetry analysis of the Γ point phonons confirm assignments from [20] with one exception—we find that the Raman mode A_{1g} (271 cm^{-1}) has a higher frequency than the IR-active mode with E_u symmetry (258 cm^{-1}). This Raman frequency agrees very well with the results for pure t-ZrO_2 [4, 26, 36]. The assignment described in table 3 is essentially equivalent to an earlier suggestion [43] and it finally disproves an alternative assignment from [38].

4. The pressure-induced transition to the cubic phase

The results presented in the previous section illustrate the level of accuracy achievable in DFT calculations of ground state properties of tetragonal zirconia. The main motivation of the present study is to extend such calculations to explain the changes of structure and properties under compression that potentially lead to a phase transition.

4.1. Structural changes under pressure

Calculated pressure–volume data for t-ZrO_2 in the pressure range from 0 to 30 GPa were fitted using the third-order Birch–Murnaghan EOS [22]. Equation of state parameters are $B = 200(2)$ GPa and $B' = 5.5(1)$. This result agrees well with the experimental and LDA results (table A.2).

Figure 1 shows the calculated pressure dependence of the two distortion characteristics that can be considered as order parameters of a phase transition under compression. LDA results predict that the cell can be described as cubic at about 40 GPa with an abrupt change taking place at 35 GPa. There is no anomalous behaviour at lower pressures; both curves in figure 1 are smooth up to about 32 GPa. It has been suggested on the basis of comparative studies of impurity-stabilized t-ZrO_2 compounds that there is a simple quadratic relationship between A and d_z, namely $A = 9.08 d_z^2$ [44]. We show in figure 2 that high pressure results for t-ZrO_2 approximately follow this dependence, with a slightly different proportionality coefficient of 8.3(1). This implies that the main effect of introducing different stabilizing ions (e.g., Y or Ce) in various concentrations can be explained by an internal pressure due to the size effect (including that of accompanying vacancies), while a chemical effect plays a secondary role in defining the tetragonal distortion of stabilized zirconia.

An x-ray diffraction study of nanocrystalline ZrO_2 reported that at about 8 GPa the A ratio became nearly 1 [5]. On the other hand, in the same experiment the value of d_z decreased much more slowly, so the pressure point of 8 GPa was not interpreted as a phase transition pressure. Even though the cell parameters could be presented as being metrically cubic, the internal coordinates of O atoms were shifted from the ideal cubic positions of the fluorite structure. Above 30 GPa it was possible to refine the experimental data using either a tetragonal or cubic description of the cell [5]. It was

Table 3. Phonon frequencies of tetragonal ZrO_2. Assignments of experimental results follow analysis from [20]; the two modes marked with [§] were incorrectly assigned in [20].

Mode	IR	Raman	LDA[a]	LDA[b]	GGA[c]	Exp.[d]	Exp.[e]	Exp.[f]	Exp.[g]	Exp.[h]	Exp.[i]	LDA[j]
E_g		Y	146.7		126		155		150	149	146	139.2
E_u TO	Y		152.7	154	76	164		140				142.9
E_u LO	Y		259.1 [§]			232						257.6
A_{1g}		Y	270.5 [§]		286		266	257	262	269	267	271.4
B_{1g}		Y	330.5		290		326	305	328	319	315	319.2
A_{2u} TO	Y		338.5	334	325	339		320				335.2
E_u TO	Y		449.4	437	435	467		550				436.1
E_g		Y	473.7		411		474	465	470	461	456	452.7
B_{1g}		Y	607.0		569		616	595	609	602	607	592.5
E_g		Y	659.2		625		645	630	643	648	645	641.3
A_{2u} LO	Y		663.8			650						648.1
B_{2u}			673.4									654.4
E_u LO	Y		734.1			734						727.1

[a] NCP calculations using ABINIT [20].
[b] USP calculations; only frequencies of IR-active transverse modes are reported [14].
[c] PAW calculations using VASP [8]. [d] IR reflectance spectroscopy [42].
[e] Raman spectroscopy, 4.6 mol % Y_2O_3 [38]. [f] IR and Raman spectroscopy, yttria and ceria doped t-ZrO_2 [39].
[g] Raman spectroscopy on yttria doped t-ZrO_2; frequencies are extrapolated to 0 K [37]. [h] Raman spectroscopy, nanosized pure t-ZrO_2 [4, 36]. [i] Raman spectroscopy, nanosized pure t-ZrO_2 [26].
[j] Present results.

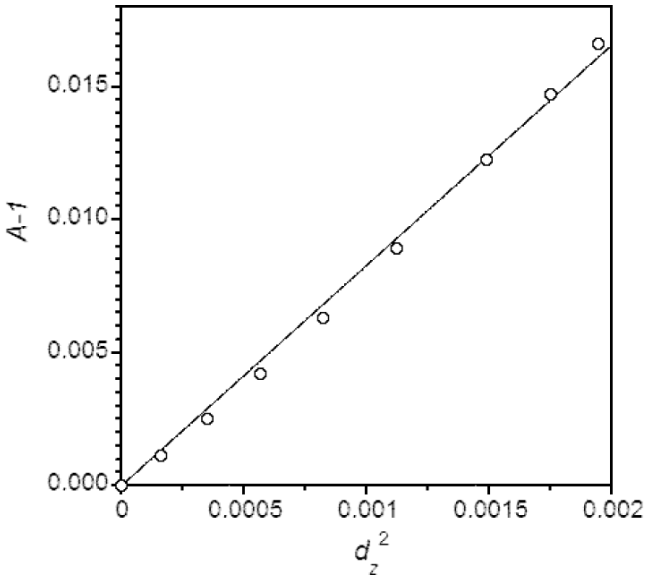

Figure 2. Correlation between two tetragonal distortion characteristics, $A - 1$ and d_z.

not possible to suggest a definitive transition pressure from the diffraction data, but our estimate of ≈37 GPa (including a 2.2 GPa thermal correction) is in good agreement with the experimental analysis. However, the observation of an anomaly at 8 GPa cannot be explained on the basis of present theoretical results and could be due to an experimental artefact such as an inhomogeneous pressure distribution inside the high pressure cell. The fact that our data follow the quadratic coupling between A and d_z (see figure 2) while experimental data from [5] strongly disagree with it further suggests a problem with the high pressure experiment.

A recent more accurate study of the structural evolution under pressure up to 18 GPa did not confirm the existence of a feature at 8 GPa [45]. A linear extrapolation of the cell parameters showed that the distortion A becomes equal to 1 at about 36 GPa. The arguments invoked in [45] to justify a linear extrapolation instead of the EOS fitting are not clear, but either way the pressure range was not sufficiently large for getting an accurate estimate of the transition point.

ZrO_8 octahedra are strongly distorted at $P = 0$, so there are two inequivalent Zr–O bonds with bond lengths of 2.072 and 2.335 Å. The Mulliken bond populations that give a qualitative assessment of the bond strength are respectively 0.62 and 0.35 in this structure. A compression towards a fluorite-type structure makes the polyhedron essentially symmetrical, and the bond populations become 0.45 for both bonds at 35 GPa. Further compression to 50 GPa preserves the cubic structure and reduces bond populations only very slightly.

4.2. Electronic structure changes under pressure

Electronic states of t-ZrO_2 can be described as follows. The valence band is comprised of a relatively narrow (2 eV wide) band of O s states at about 16 eV below the Fermi level; these states are hybridized with Zr s and p states. There is a broad band (5 eV wide) of mostly O p states that are hybridized with Zr d states at the top of the valence band. The lowest conduction band is mostly of Zr d character. We find the band gap at $P = 0$ to be indirect with the value of 3.73 eV. Experimental results for the band gap of t-ZrO_2 are 4.2 eV from electron energy-loss spectroscopy (EELS) [46] and 5.78–6.62 eV from vacuum-ultraviolet (VUV) absorption spectroscopy [47]. One should note that the EELS value gives at best an estimate of a single-particle band gap [48], so the VUV result is more reliable despite the large uncertainty of the VUV band gap [47].

The underestimation of the band gap observed here is typical of Kohn–Sham DFT calculations. Other published

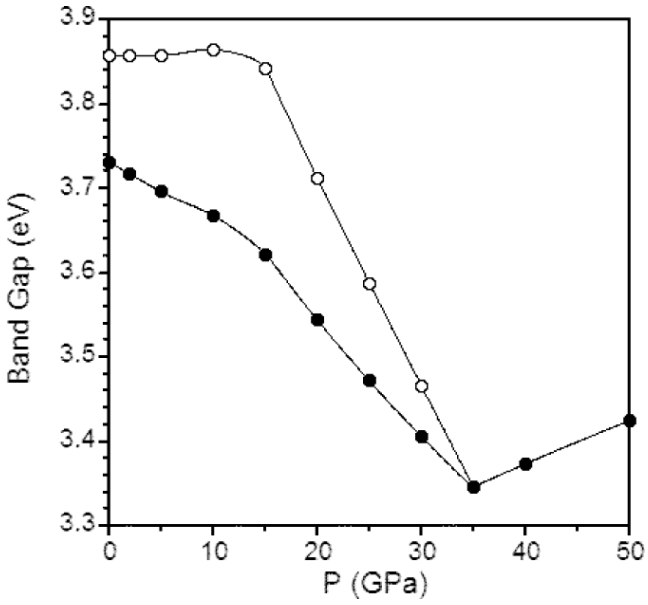

Figure 3. Pressure dependence of the indirect (solid circles) and direct (open circles) band gaps. A quasi-harmonic correction of 2.2 GPa (at 300 K) is not included in the pressure.

LDA values of a band gap are 4.10 eV [49], 4.0 eV [48], 3.85 eV [16] and 3.93 eV [50], while GGA calculations produced similar values of 3.95 eV [51], 3.90 eV [16], 4.21 eV [52], 3.7 eV [34], and 3.17 eV [21]. It is possible to improve the description of the band gap by using more advanced treatments such as invoking a screened exchange formalism. This approach produces an indirect band gap of 5.95 eV but otherwise does not introduce qualitative changes to the calculated band structure [50]. An approximate application of a more sophisticated GW method gives an even higher value of the band gap, 6.40 eV [49].

The band gap in the tetragonal phase changes its character under compression. The conduction band minimum, CBM, remains at the zone centre Γ in all calculations. The valence band maximum, VBM, is at the point A (1/2 1/2 1/2) for pressures below 15 GPa. The indirect band gap decreases on compression, and the low pressure part of the dependence shown in figure 3 can be described using a linear fit with a slope of -6.3 meV GPa^{-1}.

The inflection point at 15 GPa can be seen in figure 3. At this pressure the VBM is located in the middle of the A–M path, where M is the (1/2 1/2 0) point. VBM moves to the point M at pressures above 15 GPa. High pressure structures starting from the 35 GPa point produce essentially equivalent values for the valence band maxima at M and Γ which is easily understood as these two points are equivalent in a cubic cell. The band gap after the transition at 35 GPa shows a linear increase with pressure with a slope of 5.2 meV GPa^{-1}.

The main changes in the electron density of states, DOS, upon compression can be described as a widening of all the bands. The width of the valence and conduction bands increases by approximately 50% at 40 GPa relative to the ambient conditions. This applies also to the localized Zr 4p states that nominally could be considered as core states. Their contribution to the DOS has a noticeable dispersion even at $P = 0$, creating a peak at -25 eV which is approximately 1 eV wide. This peak becomes even more dispersive at 40 GPa, and it starts showing strong hybridization with O s states. This observation of the chemical activity of Zr 4p states shows that it was essential to include semicore states of Zr explicitly in the calculation.

4.3. Born effective charge tensors and dielectric tensors under pressure

The pressure dependence of the symmetrically inequivalent components of the Born effective charge tensors on O and Zr atoms is presented in figure 4. The Born effective charges for the pseudo-cubic structure obtained at 40 GPa are essentially isotropic with the values of 5.94 for Zr and -2.97 for O (the ratio has to be exactly -2 as a result of the acoustic sum rule). The charges calculated for cubic zirconia at ambient conditions [14] are 5.72 and -2.86, respectively. It is clear from figure 4 that the anisotropy of Born effective charge tensors decreases under compression and essentially disappears at the point of transition to fluorite structure.

The large changes in calculated Born effective charges are in stark contrast to the behaviour of the Mulliken charges that are commonly used as a qualitative measure of the charge transfer. Mulliken charges in tetragonal zirconia are completely independent of pressure, with values of -0.73 (O) and 1.46 (Zr) from 0 to 50 GPa.

The pressure dependence of the dielectric permittivity is given in figure 5. The static permittivity calculated for the cubic structure above the transition pressure, ∼26, is noticeably lower than the reported permittivity of cubic zirconia at ambient conditions, $\varepsilon^0 = 35.5$ [20]. At the same time the average value of the optical permittivity increases on compression, albeit slightly. The difference of the pressure effects on the lattice contributions to the parallel, ε^0_{zz}, and perpendicular, ε^0_{xx}, components of the static dielectric permittivity can be explained by the nature of the contributing vibrations. The ε^0_{xx} contribution is due to two E_u modes, while ε^0_{zz} is due to the A_{2u} mode. The contributions are linearly proportional to the mode oscillator strength and inversely proportional to the square of the mode frequency. This implies that in most cases the dielectric permittivity is determined by the low frequency IR-active modes. The oscillator strength of the A_{2u} mode increases under pressure faster than the square of the mode frequency, hence the overall increase in the ε^0_{zz} values. The frequency of the lowest E_u mode, on the other hand, increases very rapidly upon compression which leads to a drop in the ε^0_{xx} values.

4.4. Phonon frequencies at the Γ point under pressure

High quality Raman spectra are available from diamond anvil cell experiments on nanosized pure t-ZrO_2 crystals in the pressure range from 0 to 31 GPa [4]. The results show that at low pressure all Raman frequencies change linearly with the slopes given in table 4 (these values are related to the mode Grüneisen coefficients, $\gamma_i = -\partial \ln v_i / \partial \ln V$). Calculated LDA values are in good quantitative agreement with experiment, thus confirming the high accuracy achievable in

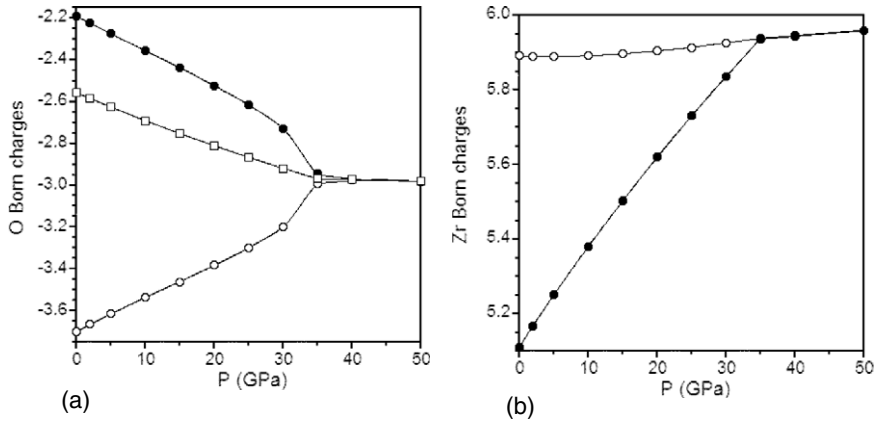

Figure 4. Pressure dependence of Born effective charges on (a) oxygen and (b) zirconium; Z_{11}^{*O}—open circles, Z_{22}^{*O}, Z_{33}^{*Zr}—solid circles, Z_{33}^{*O}—open squares. A quasi-harmonic correction of 2.2 GPa (at 300 K) is not included in the pressure.

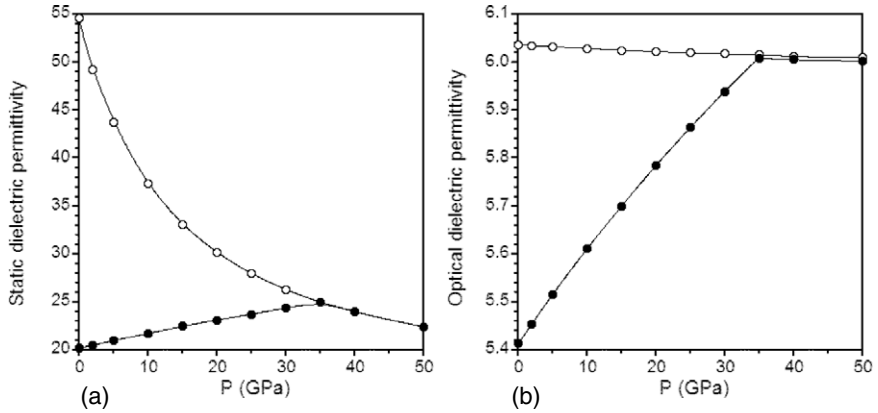

Figure 5. Pressure dependence of the (a) static and (b) optical dielectric permittivity; ε_{xx}—open circles, ε_{zz}—solid circles. A quasi-harmonic correction of 2.2 GPa (at 300 K) is not included in the pressure.

Table 4. Linear fit of Raman frequencies for pressures below 10 GPa, $v = v_0 + \frac{P\partial v}{\partial P}$.

v_0 (cm^{-1})		$\partial v/\partial P$ (cm^{-1} GPa^{-1})	
Experiment[a]	LDA[b]	Experiment[a]	LDA[b]
149.2	139.6	1.75	1.49
269.4	272.1	−3.59	−3.77
319.4	319.9	3.43	3.03
461.6	452.7	5.58	5.14
602.5	592.8	2.41	2.53
648.5	641.8	2.79	2.30

[a] Experimental data from [4].
[b] Present results.

theoretical modelling of such sensitive properties. All modes stiffen upon compression with the exception of the 260 cm^{-1} line, which softens. After about 10 GPa the dependence of frequencies on pressure becomes nonlinear both in the experiment [4] and in our calculations; see figure 6.

There is an intriguing question as regards the behaviour of the two lowest Raman-active branches. Experimental study assigned both of them an E_g symmetry label, and then the spectra were interpreted assuming a non-crossing behaviour for these two modes. The authors state that there is an exchange of the intrinsic character, namely of the peak width, of the two modes at 21 GPa, although it was claimed that the modes cannot actually cross for symmetry reasons [4]. We have presented a correct mode assignment in table 3 which agrees with e.g. [43] and confirms that these two modes are of different symmetries. According to the symmetry analysis one of these modes has a two-dimensional representation (E_g, the lowest mode at $P = 0$) while the other is one dimensional (A_{1g}), and there is no symmetry argument against crossing of these two branches. We predict this crossing to occur at 25 GPa (including quasi-harmonic correction), close to the experimental estimate of 21 GPa for the 'exchange of character' point.

The softening of the 260 cm^{-1} mode in the pressure range from 0 to 30 GPa has been fitted using a power law $v = a(P_c - P)^b$ [4]. The result of the fitting of experimental data predicted a possible phase transition at $P_c = 38$ GPa where the frequency would become zero. A similar fitting of our data predicts a complete softening at a slightly lower pressure of 36.7(2) GPa including a 2.2 GPa quasi-harmonic correction. This conclusion is confirmed quite accurately by inspection of the calculated frequencies at higher pressures; see figure 6(a). There is a clear discontinuity in three branches,

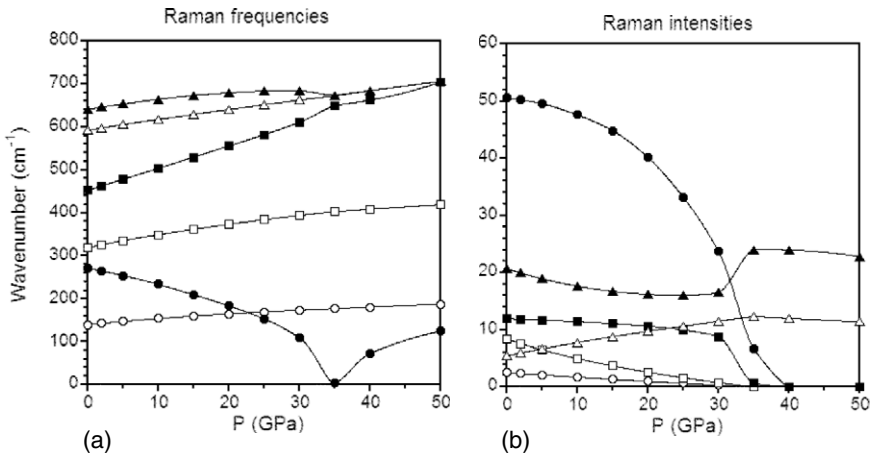

Figure 6. Calculated pressure dependence of Raman frequencies (a) and intensities (b). The symbols in the two charts correspond to the same phonon branches. The solid line with no symbols represents the combined intensity of two high frequency modes. A quasi-harmonic correction of 2.2 GPa (at 300 K) is not included in the pressure.

and most prominently there is a strong dip of the A_{1g} branch to essentially zero frequency.

A very detailed symmetry analysis of a possible symmetry change under pressure has been offered in [45]. The underlying assumption was again that the two lowest modes do not cross under compression and hence are of the same E_g symmetry. The conclusion was that the highest frequency mode at 639 cm^{-1} is the soft mode of A_{1g} symmetry. Furthermore, it was suggested that there is a new intermediate tetragonal phase (space group 136, $Z = 4$) which is achieved under compression—and this new phase then further transforms into a cubic phase. We find it difficult to see how the highest Raman-active mode could be responsible for a soft mode transition. There is indeed a slight softening of that mode at the phase transition point of 35 GPa (figure 6(a)) but it is quite clear from the actual symmetry analysis that it is the 260 cm^{-1} mode which has an A_{1g} character, which softens to zero frequency and is thus responsible for the tetragonal to cubic transition.

The frequencies of the three high frequency Raman-active modes as extrapolated in the experimental study would converge at approximately 650 cm^{-1} 'at high pressures' [4]. This statement has to be qualified for 'high pressures' to mean a point at about 35 GPa where tetragonal distortions disappear. Our calculated frequencies agree with the estimate, and even such fine detail as a decrease of the highest frequency E_g mode before the transition is faithfully reproduced.

4.5. Raman intensities at ambient conditions and under pressure

There have been a number of reports of the Raman spectra of tetragonal zirconia at zero pressure. These include studies of pure nanosized powders [4, 26, 27, 36] as well as yttria-stabilized samples [37, 39]. Quantitative data on relative intensities of various lines are invariably noisy since the lines are fairly broad in nanosized powders and often have to be separated from the spectrum of the monoclinic phase, but there seems to be a consensus that the A_{1g} line at 260 cm^{-1} is the strongest, followed by the high frequency E_g mode.

There is an experimentally observed global loss of intensity in Raman spectra above 24 GPa. The spectrum moves towards a single line at about 700 cm^{-1}, although the spectrum at 31 GPa still shows a split high frequency peak, so the structure is not yet cubic at that pressure [4].

Calculated Raman spectra are shown in figure 7 in comparison with the experimental spectra [4]. Note that we analyse Raman intensities, not Raman activities [24], so the results presented in figure 7(b) should be directly comparable to experiment. The spectra were produced by applying an instrumental broadening of 10 cm^{-1} and by using a low temperature limit in the Raman intensity calculations [24].

The soft mode at 260 cm^{-1} is the strongest feature in the spectrum at zero pressure; its intensity is twice as large as the combined intensities of the two high frequency modes, both in our calculations (figure 6(b)) and in experiment [4, 26]. The intensity of the soft mode decreases monotonically under compression and falls to zero upon transition to the cubic modification. At the same time the intensity of the high frequency features increases as a result of a monotonic increase of the intensity of the B_{1g} line combined with the jump of the E_g mode intensity at the phase transition point. The pressure dependence of the combined intensity of these two modes, as shown in figure 6(b), is qualitatively similar to the experimental observation [4].

5. Conclusions

We presented a comprehensive study of the structure and properties of tetragonal zirconia at ambient conditions and under compression up to 50 GPa. Our results strongly suggest that tetragonal distortions disappear at 37 GPa and the structure can be described as a fluorite-type cubic modification at higher pressures. The transition manifests itself clearly in the pressure dependence of tetragonal distortion parameters, Born effective charges, the dielectric permittivity, and the electronic band gap. The frequency of the A_{1g} mode, the strongest line in the Raman spectrum at $P = 0$ GPa, softens under pressure according

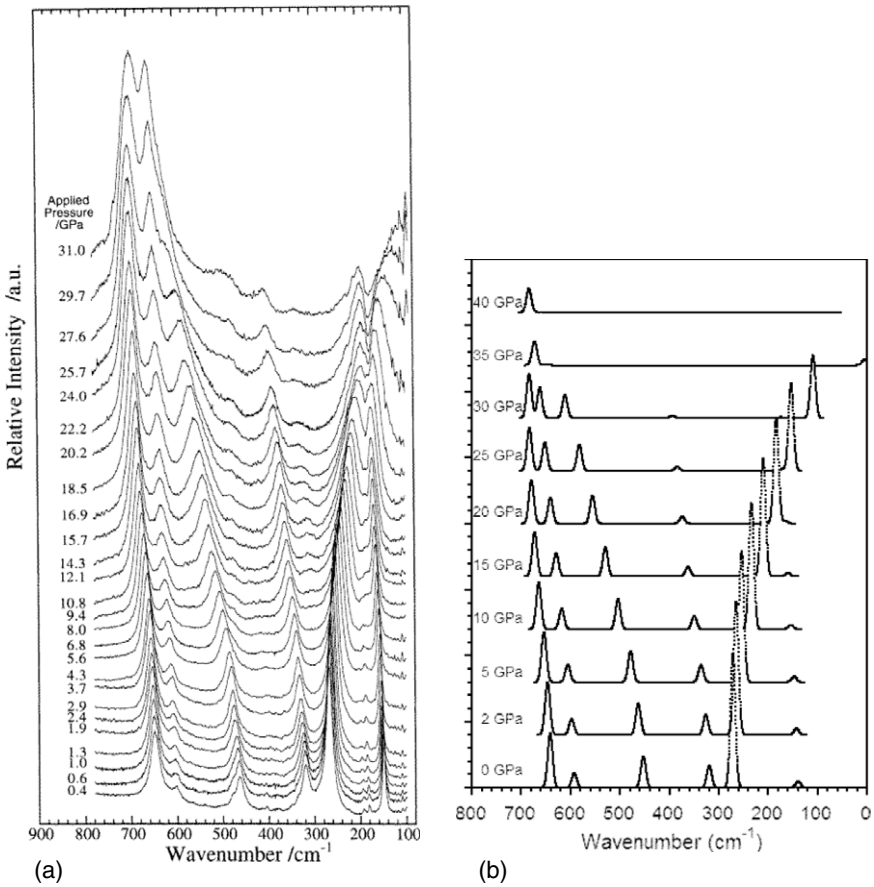

Figure 7. Pressure dependence of Raman spectra; (a) experiment (reprinted from [4] with permission from Elsevier), (b) present calculation.

to the power law and goes to zero at the transition point; its intensity also decreases.

The structure remains cubic upon further compression to 50 GPa. We have seen no indication for the presence of an additional intermediate tetragonal phase in the pressure range 10–40 GPa that had been suggested earlier [45]. There are qualitative changes in the electronic structure of the tetragonal phase related to the shift of the position of the valence band maximum, but this change does not have an apparent effect on measurable physical properties. For example, calculated optical properties such as a frequency-dependent refractive index that should be sensitive to details of the electronic structure do not exhibit any qualitative changes over the pressure range 0–50 GPa. Our results do not allow us to exclude definitively the possibility of the presence of such an extra phase ($P4_2/mnm, Z = 4$) since there is no displacive path that connects it to the known tetragonal phase studied here ($P4_2/nmc, Z = 2$) and so we could not obtain this structure by simply applying pressure to the known modification. Its existence is however rather unlikely since it was deduced on the basis of an erroneous symmetry analysis of soft mode behaviour and incorrect symmetry assignments [45]. An attempt to generate such a structure followed by geometry optimization showed that it spontaneously transforms to cubic symmetry and thus it is not even a metastable configuration.

One should observe that the agreement of the calculated phase transition pressure, 35 GPa, with the experimental estimate of 30 GPa [5] may be slightly fortuitous, or it might imply that the material inside nanograins represents a nearly perfect metastable t-ZrO_2 with a minimal effect of residual strain.

In summary, we presented the first *ab initio* description of pressure-induced changes in the Raman spectrum of tetragonal zirconia and showed the relationship between these changes and the structural phase transformation.

Appendix

We present here a compilation of experimental and theoretical results relating to the structure and elasticity of tetragonal zirconia. The first experimentally reported structure of pure t-ZrO_2 was recorded at 1250 °C using single-crystal x-ray diffraction [11]. The most accurate room temperature x-ray diffraction structure determination of chemically pure t-ZrO_2 obtained by the spray-pyrolysis technique was reported in [4]. Neutron powder diffraction of pure t-ZrO_2 at room temperature was used with samples prepared by the alkoxide method [25]; the results can be compared to neutron powder diffraction analysis of yttria-stabilized t-ZrO_2 [28]. Neutron diffraction was used to obtain the structure of nanocrystalline powders down to cryogenic temperatures; we included in table A.1 the lowest temperature data obtained at 5 K for samples with the grain size of 13 nm [27].

Table A.1. Structure of tetragonal ZrO_2 from experiment and DFT. The name of the DFT package is indicated where known. N_k is the number of irreducible k-points where the Monkhorst–Pack scheme was used; E_{cut} is the energy cut-off in eV for plane wave based methods.

Method	N_k	E_{cut}	a (Å)	c (Å)	A	d_z
Experiment (x-ray diffraction)[a]			3.5958	5.187	1.020	0.045
Experiment (neutron diffraction)[b]			3.6055	5.1797	1.016	0.041 3
Experiment (neutron diffraction)[c]			3.591	5.169	1.018	0.041
Experiment (x-ray diffraction)[d]			3.64	5.27	1.024	0.065
Experiment (neutron diffraction)[e]			3.574	5.154	1.020	0.047
LDA[f]			3.57	5.08	1.006	0.029
LDA[g]	6	1360	3.563	5.104	1.013	0.042
LDA[h]	40		3.590	5.227	1.030	0.060
LDA[i]	18	950	3.59	5.15	1.014	0.042
LDA[j]	12	816	3.55	5.09	1.014	0.040
LDA[k]	84	800	3.583	5.140	1.014	0.041
LDA[l]	12	340	3.5567	5.1044	1.014	0.041 8
LDA[m]		2300	3.5645	5.1258	1.017	0.044 1
LDA[n]	30	750	3.5654	5.1259	1.017	0.044 1
GGA[0]	40		3.654	5.364	1.038	0.050
GGA[p]	216	250	3.645	5.289	1.026	0.054
GGA[q]	12	500	3.642	5.295	1.028	0.054
GGA[r]	75		3.61	5.25	1.028	0.047
GGA[s]	12		3.642	5.275	1.024	0.051 5
GGA[t]	12	1632	3.622	5.284	1.032	0.057 25
GGA[u]	45	476	3.61	5.20	1.019	

[a] Pure nanocrystalline t-ZrO_2 [4]. [b] Yttria doped t-ZrO_2 [28]. [c] Pure t-ZrO_2 [25].
[d] Pure t-ZrO_2 at high temperature [11]. [e] Pure t-ZrO_2, $T = 5$ K [27]. [f] FLAPW [53].
[g] NCP [49]. [h] USP (VASP) [16]. [i] NCP (CPMD) [54]. [j] NCP (ABINIT) [20].
[k] PAW (VASP) [35]. [l] USP [14]. [m] NCP (PWSCF) [48]. [n] NCP, present result.
[o] USP (VASP) [16]. [p] PAW (VASP) [52]. [q] PAW (VASP) [8]. [r] FLAPW (WIEN2k) [51].
[s] USP (CASTEP) [21]. [t] PAW-USP (ABINIT) [33]. [u] NCP (SIESTA) [34].

Table A.2. Mechanical properties of tetragonal ZrO_2: the bulk modulus B and its pressure derivative B', Poisson's ratio ν, the shear modulus G, the Young modulus E.

	B (GPa)	B'	G (GPa)	E (GPa)	ν
Exp.[a]	190		80	215	0.316
Exp.[b]	198(7)				
Exp.[c]	170(10)	4.3(1.3)			
LDA[d]	200	6.25			
LDA[e]	197	5.0			
LDA[f]	207	5.0			
LDA[g]	196[h]; 204[i]		99[i]	257	0.29
LDA[j]	200(2)[h]; 223[i]	5.5	103[i]	248–320	0.15–0.59
GGA[k]	226.1	3.81			

[a] Room temperature ultrasonic measurements on yttria doped polycrystals [55].
[b] X-ray diffraction using a diamond anvil cell; pure nanocrystalline t-ZrO_2 [5].
[c] Synchrotron x-ray diffraction using a diamond anvil cell; pure nanocrystalline t-ZrO_2 [45].
[d] NCP calculations [56]. [e] NCP calculations [54].
[f] NCP calculations [48]. [g] PAW calculations [35].
[h] Extracted from EOS calculations (third-order Birch–Murnaghan equation).
[i] Polycrystalline Voigt average.
[j] Present results; the values for E and ν are the limits of orientation-dependent single-crystal data.
[k] GGA; all-electron FLAPW calculations [51].

Table A.3. Single-crystal elastic constants of tetragonal ZrO_2 (GPa). The bulk modulus, B, is derived from the C_{ij} tensor.

	C_{11}	C_{33}	C_{44}	C_{66}	C_{12}	C_{13}	B
Exp.[a]	327	264	59	64	100	62	149
SC-TB[b]	366	286	78	88	180	80	190
PIB[c]	465	326	101	156	83	49	179
GGA[d]	293	385	51	187	248	111	210
GGA[e]	334	248	9.08	152	211	51.9	172
LDA[f]	382	346	42	167	221	72	204
LDA[g]	401(3)	345(2)	49(3)	174(1)	245(2)	90(5)	212(2)

[a] Neutron powder diffraction for 12 mol% Ce doped t-ZrO_2 [32].
[b] Self-consistent tight-binding model [57].
[c] Potential-induced breathing model [58].
[d] NCP calculations [34]. [e] PAW-USP calculations [33].
[f] PAW calculations [35]. [g] Present results.

Available experimental and DFT results for mechanical properties of tetragonal ZrO_2 are presented in table A.2. The bulk modulus values were obtained mostly from high pressure compressibility experiments, either by using a diamond anvil cell or by using DFT to calculate the equation of state. The low quality of the fit for the measured EOSs is illustrated by large statistical uncertainties [5, 45], so one still does not have an accurate experimental estimate of the t-ZrO_2 bulk modulus.

The theoretical and experimental results for single-crystal elastic constants of t-ZrO_2 are summarized in table A.3. Experimental values of elastic constants are the first reported

results from determining elastic constants of anisotropic materials using powder diffraction measurements [32]. The derivation of the C_{ij} tensor required strain–stress data as well as an estimated value of Young's modulus (taken to be 192 GPa).

References

[1] Manicone P F, Iommetti P R and Raffaelli L 2007 *J. Dent.* **35** 819–26
[2] Bocanegra-Bernal M H and De la Torre S D 2002 *J. Mater. Sci.* **37** 4947–71
[3] Kelly P M and Rose L R F 2002 *Prog. Mater. Sci.* **47** 463–557
[4] Bouvier P and Lucazeau G 2000 *J. Phys. Chem. Solids* **61** 569–78
[5] Bouvier P, Djurado E, Lucazeau G and Le Bihan T 2000 *Phys. Rev.* B **62** 8731–7
[6] Ohtaka O, Andrault D, Bouvier P, Schultz E and Mezouar M 2005 *J. Appl. Crystallogr.* **38** 727–33
[7] Jaffe J E, Bachorz R A and Gutowski M 2005 *Phys. Rev.* B **72** 144107
[8] Kuwabara A, Tohei T, Yamamoto T and Tanaka I 2005 *Phys. Rev.* B **71** 064301
[9] Rignanese G M 2005 *J. Phys.: Condens. Matter* **17** R357–79
[10] Hahn T 1989 *International Tables for Crystallography* vol A (Dordrecht: Kluwer)
[11] Teufer G 1962 *Acta Crystallogr.* **15** 1187
[12] Clark S J, Segall M D, Pickard C J, Hasnip P J, Probert M I J, Refson K and Payne M C 2005 *Z. Kristallogr.* **220** 567–70
[13] Accelrys 2008 *Materials Studio 4.4*
[14] Zhao X and Vanderbilt D 2002 *Phys. Rev.* B **65** 075105
[15] Zhao X and Vanderbilt D 2002 *Phys. Rev.* B **65** 233106
[16] Jomard G, Petit T, Pasturel A, Magaud L, Kresse G and Hafner J 1999 *Phys. Rev.* B **59** 4044–52
[17] Rappe A M, Rabe K M, Kaxiras E and Joannopoulos J D 1990 *Phys. Rev.* B **41** 1227–30
[18] Ramer N J and Rappe A M 1999 *Phys. Rev.* B **59** 12471–8
[19] Monkhorst H J and Pack J D 1976 *Phys. Rev.* B **13** 5188–92
[20] Rignanese G M, Detraux F, Gonze X and Pasquarello A 2001 *Phys. Rev.* B **64** 134301
[21] Fan Q, Wang F, Zhang H and Zhang F 2008 *Mol. Simul.* **34** 1099–103
[22] Birch F 1947 *Phys. Rev.* **71** 809–24
[23] Refson K, Tulip P R and Clark S J 2006 *Phys. Rev.* B **73** 155114
[24] Porezag D and Pederson M R 1996 *Phys. Rev.* B **54** 7830–6
[25] Igawa N, Ishii Y, Nagasaki T, Morii Y, Funahashi S and Ohno H 1993 *J. Am. Ceram. Soc.* **76** 2673–6
[26] Barberis P, Merle-Méjean T and Quintard P 1997 *J. Nucl. Mater.* **246** 232–43
[27] Bouvier P, Djurado E, Ritter C, Dianoux A J and Lucazeau G 2001 *Int. J. Inorg. Mater.* **3** 647–54
[28] Howard C J, Hill R J and Reichert B E 1988 *Acta Crystallogr.* B **44** 116–20
[29] Djurado E, Bouvier P and Lucazeau G 2000 *J. Solid State Chem.* **149** 399–407
[30] Baldinozzi G, Simeone D, Gosset D and Dutheil M 2003 *Phys. Rev. Lett.* **90** 216103
[31] Milman V and Warren M C 2001 *J. Phys.: Condens. Matter* **13** 241–51
[32] Kisi E H and Howard C J 1998 *J. Am. Ceram. Soc.* **81** 1682–4
[33] Fadda G, Colombo L and Zanzotto G 2009 *Phys. Rev.* B **79** 214102
[34] Natanzon Y, Boniecki M and Lodziana Z 2009 *J. Phys. Chem. Solids* **70** 15–9
[35] Lowther J E 2006 *Phys. Rev.* B **73** 134110
[36] Bouvier P, Gupta H C and Lucazeau G 2001 *J. Phys. Chem. Solids* **62** 873–9
[37] Lughi V and Clarke R D 2007 *J. Appl. Phys.* **101** 053524
[38] Feinberg A and Perry C H 1981 *J. Phys. Chem. Solids* **42** 513–8
[39] Hirata T, Asari E and Kitajima M 1994 *J. Solid State Chem.* **110** 201–7
[40] Mirgorodsky A P and Quintard P E 1999 *J. Am. Ceram. Soc.* **82** 3121–4
[41] Kroumova E, Aroyo M I, Perez-Mato J M, Kirov A, Capillas C, Ivantchev S and Wondratschek H 2003 *Phase Transit.* **76** 155–70
[42] Pecharroman C, Ocana M and Serna C J 1996 *J. Appl. Phys.* **80** 3479–83
[43] Quintard P E, Barbéris P, Mirgorodsky A P and Merle-Méjean T 2002 *J. Am. Ceram. Soc.* **85** 1745–9
[44] Howard C J, Hunter B A and Kim D-J 1998 *J. Am. Ceram. Soc.* **81** 241–3
[45] Bouvier P, Dmitriev V and Lucazeau G 2003 *Eur. Phys. J.* B **35** 301–9
[46] McComb D W 1996 *Phys. Rev.* B **54** 7094–102
[47] French R H, Glass S J, Ohuchi F S, Xu Y N and Ching W Y 1994 *Phys. Rev.* B **49** 5133–41
[48] Dash L K, Vast N, Baranek P, Cheynet M-C and Reining L 2004 *Phys. Rev.* B **70** 245116
[49] Králik B, Chang E K and Louie S G 1998 *Phys. Rev.* B **57** 7027–36
[50] Medvedeva J E, Freeman A J, Geller C B and Rishel D M 2007 *Phys. Rev.* B **76** 235115
[51] Terki R, Bertrand G, Aourag H and Coddet C 2006 *Mater. Sci. Semicond. Process* **9** 1006–13
[52] Eichler A 2001 *Phys. Rev.* B **64** 174103
[53] Jansen H J F 1991 *Phys. Rev.* B **43** 7267–78
[54] Stapper G, Bernasconi M, Nicoloso N and Parrinello M 1999 *Phys. Rev.* B **59** 797–810
[55] Fukuhara M and Yamauchi I 1993 *J. Mater. Sci.* **28** 4681–8
[56] Dewhurst J K and Lowther J E 1998 *Phys. Rev.* B **57** 741–7
[57] Fabris S, Paxton A T and Finnis M W 2000 *Phys. Rev.* B **61** 6617–30
[58] Cohen R E, Mehl M J and Boyer L L 1988 *Physica* B+C **150** 1–9